

Research Article

<https://doi.org/10.1631/jzus.A2300301>

Effect of streamlined nose length on aerodynamic performances of high-speed train with speed of 400 km/h

Nianxun LI, Tian LI[✉], Zhiyuan DAI, Deng QIN, Jiye ZHANG

State Key Laboratory of Rail Transit Vehicle System, Southwest Jiaotong University, Chengdu 610031, China

Abstract: The streamlined nose length plays a crucial role in determining the aerodynamic performance of high-speed trains. An appropriate streamlined nose length can not only effectively reduce the magnitude of aerodynamic drag and lift forces, but it can also improve the performance of the high-speed train in tunnel passing and crosswind circumstances. In this study, a numerical simulation of the aerodynamic performance of high-speed trains at a speed of 400 km/h, with varying streamlined nose lengths, is conducted using the $k-\omega$ Shear Stress Transport turbulence model. The different streamlined nose lengths include 6, 7, 8, 9, 9.8, 12, 15, and 18 meters. In order to validate the accuracy of the numerical simulation, its results are compared with wind tunnel test data obtained from the literature. Numerical simulation is carried out using compressible and incompressible gases to determine the effect of gas compressibility on results. The impact of streamlined nose length on the aerodynamic performance of the trains is analyzed in terms of aerodynamic forces, velocity, and pressure distributions. In comparison to the original train, the train with a 6 m streamlined nose length experienced a 10.8% increase in overall aerodynamic resistance. Additionally, the lift forces on the head car and tail car increased by 35.7% and 75.5% respectively. On the other hand, the train with an 18 m streamlined nose length exhibited a 16.5% decrease in aerodynamic drag. Furthermore, the lift forces on the head car and tail car decreased by 21.9% and 49.7% respectively. The aerodynamic drag force of the entire train varies linearly with the streamlined nose length, while the aerodynamic lift of the tail car follows a quadratic function in relation to the streamlined nose length.

Key words: Streamlined nose length; High-speed train; Aerodynamic performance; Numerical simulation; Flow structures


1 Introduction

As the speed of a train increases and the operating environment becomes harsher (Shao et al., 2011; Xiong et al., 2011; Miao et al., 2023), several aerodynamic challenges become increasingly significant. These challenges include aerodynamic resistance, acoustic considerations and crosswind stability (Raghunathan et al., 2002; Li et al., 2013). In the context of developing the CR450 high-speed Electric Multiple Unit (EMU) capable of reaching a speed of 400 km/h, it is important to optimize its aerodynamic shape.

The aerodynamic performance of high-speed trains is greatly influenced by the design of the head

car (Li et al., 2023; Dai et al., 2023). Consequently, researchers worldwide have been studying the effects of head car shapes on aerodynamic performance. Yu et al. (2013) developed a 3D parameter model for trains, considering aerodynamic resistance and load reduction coefficient as the primary optimization objectives, conducted a correlation analysis between optimization variables and optimization objectives, and obtained the most important optimization variables. Zhang et al. (2017) focused on optimizing the aerodynamic lift of the tail car and total drag, extracted seven head shape design variables, using the non-dominated sorting genetic algorithm II (NSGA-II) and the Kriging model, creating a multi-objective aerodynamic optimization design. With the development of new types of rail transit, there is increasing research on maglev trains and some new types of ultra-high-speed trains (Britcher et al., 2012; Huang et al., 2019). Sun et al. (2021) used an improved Kriging model to optimize the aerodynamic force of the urban maglev train. The aerodynamic

✉ Tian LI, litian2008@home.swjtu.edu.cn

 Tian LI, <https://orcid.org/0000-0002-7345-7488>

noise of trains is also greatly affected by the head shape (Iglesias et al., 2017; Li et al., 2022). Based on the parametric modeling of the longitudinal line shape of the train head constructed by non-uniform rational B-splines (NURBS) and using genetic algorithms to seek the optimal solution, Xiao et al. (2014) found the resulting total pulsating pressure level is 8.7 dB lower than for the original longitudinal line shape. In order to suppress the micro pressure wave generated when the train exits a tunnel, Kikuchi et al. (2011) used the rapid computational scheme and a genetic algorithm to determine the optimal longitudinal distribution of the cross-sectional area of the train nose shape and confirmed the effect of nose shape optimization through experiments using a scale model.

The streamlined nose length (SNL) is one of the significant parameters of the shape of the train nose. Choi et al. (2014) found that, when the speed of the train doubled, changing the train's head shape from a blunt head to a streamlined head shape, could reduce the resistance of the train by 50%. In the research of Niu et al. (2018), the aerodynamic performance of high-speed trains was investigated by varying the SNLs. The study revealed that increasing the SNL of the head car from 8 m to 12 m resulted in a decrease in both the drag experienced by the tail car and the lift experienced by the head car. Chen et al. (2019) employed the Improved Delayed Detached-Eddy Simulation (IDDES) method to analyze the trackside and platform slipstream speeds of trains considering various SNLs. Chen et al. (2018) studied the aerodynamic performance of trains with different nose lengths in a strong crosswind environment. When the nose length increased from 4 m to 12 m, the total resistance decreased by 19% and the side force decreased by 10.2%. Ezoji et al. (2021) modified the basic geometric structure of the train according to the overturning conditions of the train and generated 7 new head-shaped structures, showing that increasing the length of the train nose can reduce the risk of the train overturning. Zhang et al. (2020) and Hu et al. (2022) studied the effect of train nose length on the aerodynamic performance of evacuated-tube trains and proved that under evacuated-tube operating conditions, an increase in train nose length can reduce the aerodynamic force on the train and improve its aerodynamic performance. Meng et al. (2022) studied the impact of the train nose length on the surrounding

airflow disturbance when the train passes through the noise barrier. The results showed that a longer nose length can reduce the airflow disturbance between the train and the noise barrier and ensure operational safety.

The above studies were mainly aimed at optimizing the SNL of high-speed trains operating within the speed range of 200-350 km/h. There are few studies on the aerodynamic optimization for a train at a speed of 400 km/h. Currently, the design of 400 km/h high-speed trains is being conducted in China. This study takes the high-speed EMU with a running speed of 400 km/h as the research object; the influence of different air characteristics on the numerical aerodynamic results of trains running at speeds above 400km/h is analyzed, and the formula for the change of aerodynamic force with SNL is fitted. The results can guide the optimization and development of high-speed train head shapes.

2 Numerical Information

2.1 Train Models and Calculation Conditions

The three-car high-speed train model is used to conduct numerical simulations. The train, track, and subgrade are shown in Fig. 1(a). The length of the whole train is 80 m, the lengths of the head car and the middle car are 26.85 m and 25 m respectively, the length of the tail car is the same as that of the head car, the gauge is 1.435 m, and the height and width of the track are 0.176 m and 0.05 m respectively. While maintaining the length of the head car and with the entire vehicle unchanged, the original head car with an SNL of 9.8 m is stretched and compressed to change its SNL to obtain seven different models.

Fig. 1(b) illustrates the numerical domain and boundary conditions used in the study. Four refinement zones (Refinebox0, Refinebox1, Refinebox2, Refinebox3) are established around the train to improve the mesh quality. The pressure-far-field is selected as the inlet boundary condition, with a Mach number of 0.3268 corresponding to an operating speed of 400 km/h. The turbulence intensity and hydraulic diameter are selected; the turbulence intensity is 3.0%, and the hydraulic diameter is 3.8 m. The pressure outlet is defined as the outlet boundary condition and is set to a value of zero. In the computa-

tional domain, the top and sides are considered symmetry boundary conditions. The ground and the track subgrade are set as sliding walls, and the sliding

speed is consistent with the running speed of the train, set to 111.11 m/s.

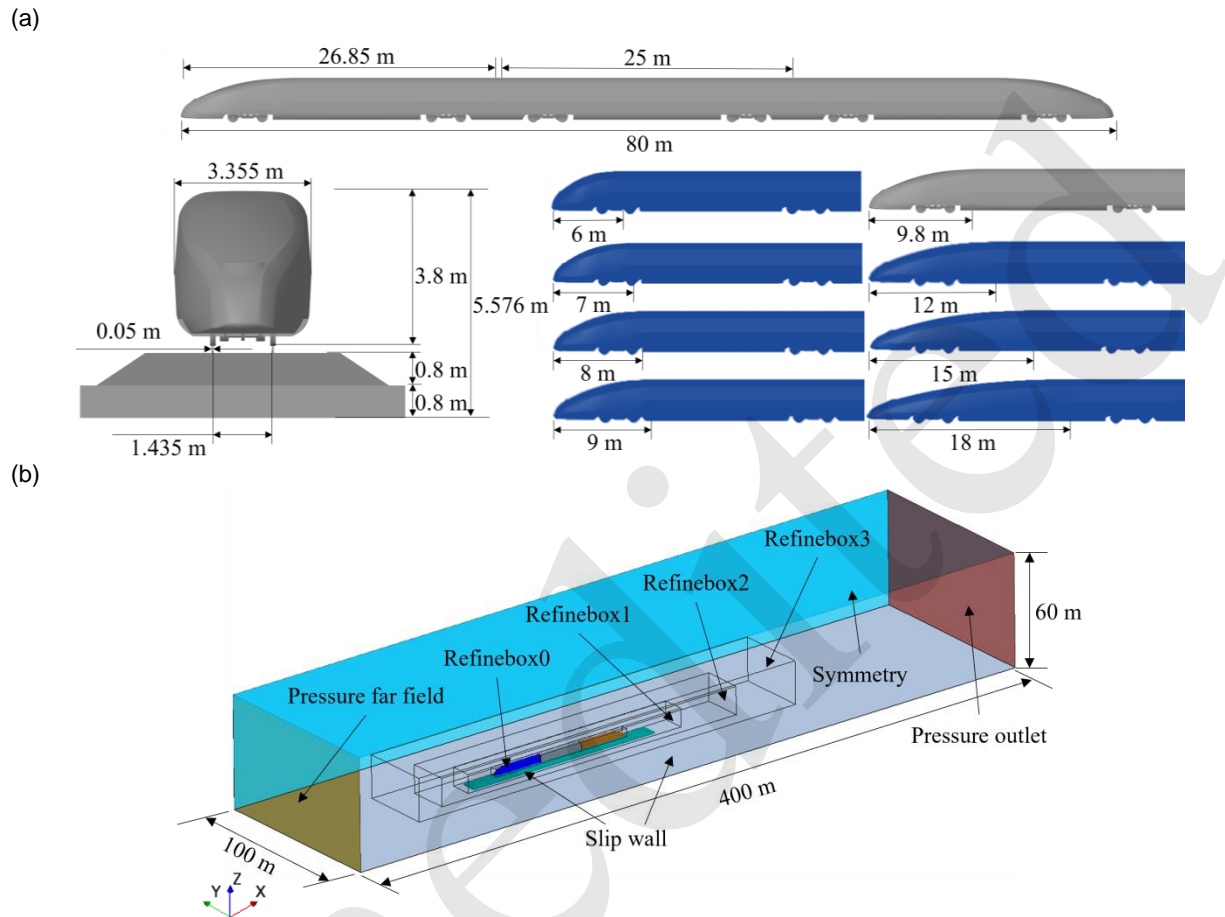


Fig. 1 Train models and the calculation conditions: (a) Train models (b) Computational domain and boundary conditions.

2.2 Numerical Method

In the research, the Mach number of the train running speed is 0.3268, which is greater than 0.3 times the speed of sound. It is necessary to consider the compressibility of air (Kim et al., 2011; Li et al., 2011), so the compressible ideal gas is used to conduct the numerical simulation. According to the research of Zampieri et al. (2020), the use of the $k-\omega$ Shear Stress Transport (SST) turbulence model in numerical simulation can better capture the turbulent structure in the boundary layer. The Semi-Implicit Method for Pressure Linked Equations (SIMPLE) algorithm is used to solve the flow field and pressure. According to the research of Liu et al. (2013), there is little difference in pantograph-catenary dynamic contact force between steady-state and unsteady-state

aerodynamic loading when the pantograph three-mass model is used for simulation. The flow around the train is unsteady when it is running. With the simplification of the train model and operating environment in this study, the use of steady-state simulation has little impact on the aerodynamic performance of the train. So the steady-state simulation is used in this study.

3 Numerical Validation

3.1 Validation of Mesh Independence

To exclude the impact of grid resolution on the accuracy of the simulation calculation, the grids are divided into coarse, medium, and fine grids, with base sizes of 1400 mm, 1200 mm, and 1100 mm, respec-

tively. The numbers of the three sets of grids are 26.75 million, 36.72 million, and 43.12 million, respectively. Fig. 2(a) displays the grid around the train and the boundary layer grid used in the simulation. Four mesh refinement zones are set to improve the mesh quality around the train. The boundary layers of the three sets of grids are the same, the thickness of the first layer is 0.01 mm, and the growth rate is 1.2, a

total of 12 layers. Fig. 2(b) shows the distribution of y^+ on the train surface of the medium grid. It can be seen that the y^+ values on the train surface are almost all less than 2. Except for part of the bogie region and the streamlined region of the head car and tail car, the y^+ values of the cells on the other train surfaces are basically around 1.

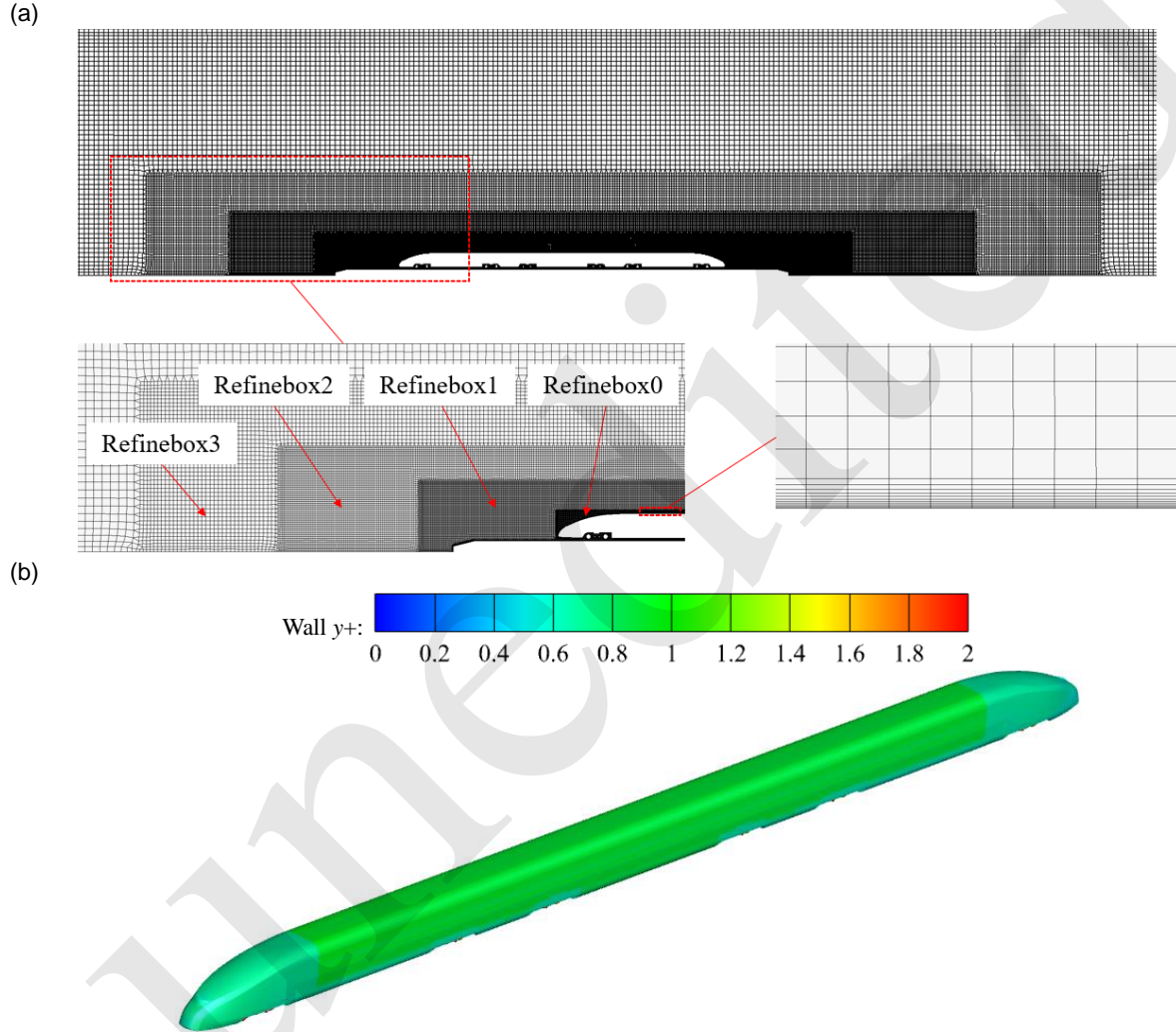


Fig. 2 Computational mesh and wall y^+ distribution: (a) Grid of computational domain and boundary layer (b) Wall y^+ distribution of the train.

The aerodynamic performance of trains is described using the dimensionless parameters C_p , C_d , and C_l , representing pressure coefficient, drag coefficient, and lift coefficient. The calculation formulas are as follows:

$$C_p = \frac{P}{0.5\rho u^2} \quad (1)$$

$$C_d = \frac{F_d}{0.5\rho u^2 A} \quad (2)$$

$$C_l = \frac{F_l}{0.5\rho u^2 A}, \quad (3)$$

where P is the surface pressure; F_d is the aerodynamic drag; F_l is the aerodynamic lift; ρ is the air density

(1.225 kg/m^3); u is the running speed; A is the windward area of the train (11.18 m^2).

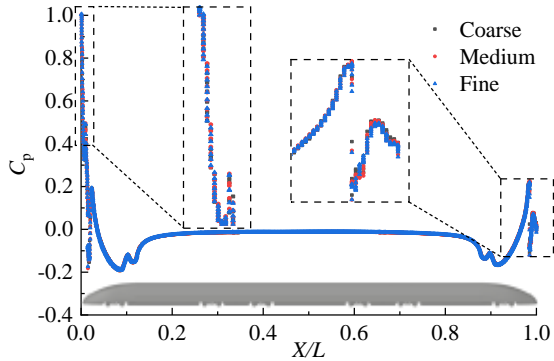


Fig. 3 Pressure coefficient distribution of $y = 0$ section

Fig. 3 shows the $y = 0$ cross-sectional pressure coefficient distribution obtained from the three sets of grid numerical simulations. In Fig. 3, X represents the distance from the front end of the head car, and L represents the length of the entire vehicle. As shown in Fig. 3, the pressure coefficient exhibits little difference in both its value and distribution. The data

comparison of the grid independence verification calculation results is shown in Table 1. The relative error between the two sets of grids gradually decreases with the increment in the number of grids. The relative error of C_d for the head car has been reduced from 1.23% to 0.85%, while the relative error of C_d for the tail car has been reduced from 1.42% to 0.46%, the relative error of the head car's lift coefficient has been reduced from 11.4% to 5.24%, and the tail car's relative error has been reduced from 3.72% to 0.86%. As the number of grids increases, the impact on the aerodynamic forces gradually diminishes. In summary, continuing to refine the grid after the number of grids reaches about 26.75 million has basically no effect on the results of numerical simulation. Considering both calculation accuracy and calculation speed, the Medium grid size is selected for follow-up research.

Table 1 Comparison table of grid independence validation

Mesh	C_d (Relative error)		C_l (Relative error)	
	Head car	Tail car	Head car	Tail car
Coarse	0.1305 (-)	0.1026 (-)	-0.0237 (-)	0.0968 (-)
Medium	0.1289 (1.23%)	0.1012 (1.42%)	-0.0210 (11.4%)	0.0932 (3.72%)
Fine	0.1300 (0.85%)	0.1016 (0.46%)	-0.0221 (5.24%)	0.0940 (0.86%)

3.2 Validation of Wind Tunnel Test

To ensure the reliability and accuracy of the numerical simulation, a comparison is made between the simulation results and the findings from wind tunnel tests that have been conducted. This validation process helps confirm the fidelity of the numerical simulation. The test adopts a scale model of 1:8, and 11 pressure measuring points are arranged in the $y = 0$ section. The data comes from the literature (Huo et al., 2021).

Fig. 4 illustrates the comparison of the aerodynamic coefficient for the head car as well as the distribution of the pressure coefficient along the $y = 0$ section. It can be seen from Fig. 4(a) that the disparity in drag coefficient between the simulation results in the literature and the wind tunnel test findings is

1.71%. The above discrepancy between the numerical simulation results presented in this study and the wind tunnel test results is less than 5%. Meanwhile, the numerical simulation results of lift force coefficients in the literature and this study are very close to the experimental data. The pressure comparison of the $y = 0$ section is shown in Fig. 4(b). X represents the distance from the front end, while L_{head} represents the length of the whole head car. The pressure coefficients on the $y = 0$ section obtained from both the test and the numerical simulation exhibit excellent agreement with only slight deviations in a few points. It can be concluded that the numerical simulation method used in this study yields reliable and accurate results.

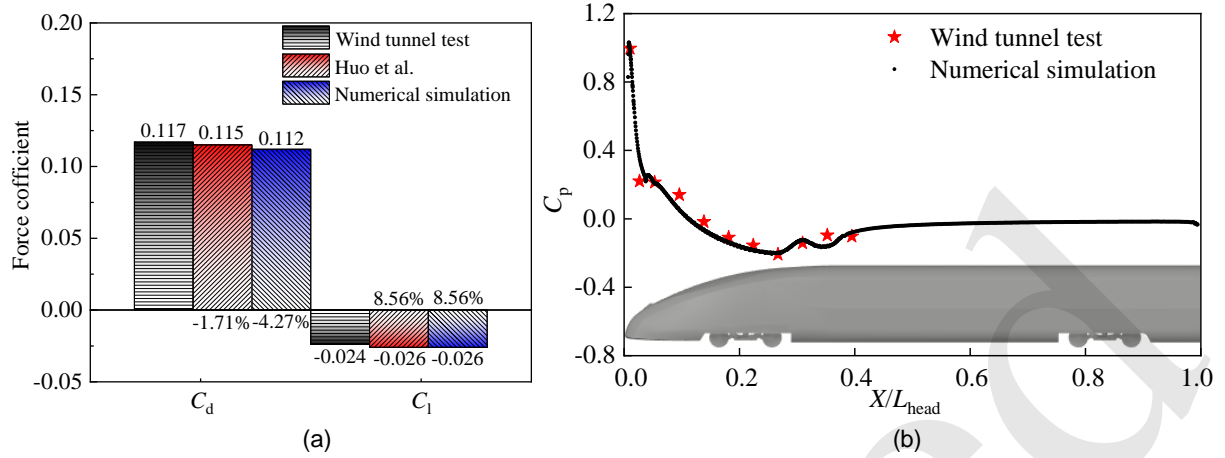


Fig. 4 Comparison of wind tunnel test and numerical simulation results: (a) Comparison of aerodynamic coefficient (b) Comparison of $y = 0$ section pressure of the head car.

3.3 Validation of the Effect of Gas Compressibility on Results

The speed of the train is 400 km/h and exceeds the Mach number of 0.3, so the compressibility of the gas cannot be ignored. In previous studies, incompressible gas was used for numerical simulation. To validate that the compressibility of gas will affect the numerical results, we use compressible gas and incompressible gas as simulation fluids to carry out the numerical simulation on a train with an original SNL of 9.8 m.

As shown in Table 2, the compressibility of the gas has a significant impact on the drag and lift force of the head car, as well as the lift force of the tail car. The numerical simulation of two different gases resulted in relative errors of 4.32% for $C_{d\text{-head}}$, 4.90% for $C_{l\text{-head}}$, and 1.47% for $C_{l\text{-tail}}$.

Table 2 Comparison of aerodynamic coefficient

Fluid characteristics	$C_{d\text{-head}}$	$C_{l\text{-head}}$	$C_{d\text{-tail}}$	$C_{l\text{-tail}}$
Compressible air	0.1289	-0.0210	0.1012	0.0932
Incompressible air	0.1347	-0.0221	0.1009	0.0919
Relative error	4.32%	4.90%	0.30%	1.47%

Fig. 5 shows the velocity and pressure coefficient distribution near the train surface on the $z = 1.5$ m section. As shown in Fig. 5(a), the speed obtained by using the incompressible gas simulation is smaller, and the maximum absolute error in speed value around the train obtained by the two kinds of gas simulation reached 3.22 m/s. Fig. 5(b) illustrates that

the difference in the distribution of the pressure coefficient is mainly reflected in the transition area of the train from streamlined to non-streamlined. In this area, the simulation results using the incompressible gas exhibit a smaller peak value of negative pressure, and the maximum absolute error in the pressure coefficient value reached 0.0083, which is converted into an aerodynamic force of about 702 N. When using the compressible gas for simulation, the airflow velocity around the train is overall greater, and the airflow velocity reaches an extreme value due to the influence of the train geometry in the area where the train changes from streamlined to non-streamlined. According to the Bernoulli principle, the greater the airflow velocity, the smaller the negative pressure generated, so the C_p of this part of the area obtained by using compressible gas for simulation is smaller.

Fig. 5(c) shows the boundary layers of the head car and the tail car. The $0.99u_{\text{inf}}$ (u_{inf} represents the velocity of inflow) is employed as the value of the boundary layer isoline. The velocity of airflow inside the isoline is less than $0.99u_{\text{inf}}$, and that of the airflow outside is greater than $0.99u_{\text{inf}}$. The simulation using an incompressible gas yields a thicker velocity boundary layer, so the average velocity near the train surface is smaller. According to Newton's law of viscosity, the viscous shear stress acting on the wall is proportional to the velocity gradient of the fluid near the wall (White and Majdalani, 2006), which causes the obtained viscous drag on the train surface to be smaller than that obtained by simulation with the compressible gas.

The train aerodynamics is investigated through numerical simulation, employing two different gases with distinct characteristics, and the results show that the compressibility of the gas has a great influence on

the numerical results. This validates the feasibility and rationality of using compressible gas in the numerical simulation of train aerodynamic performance in this study.

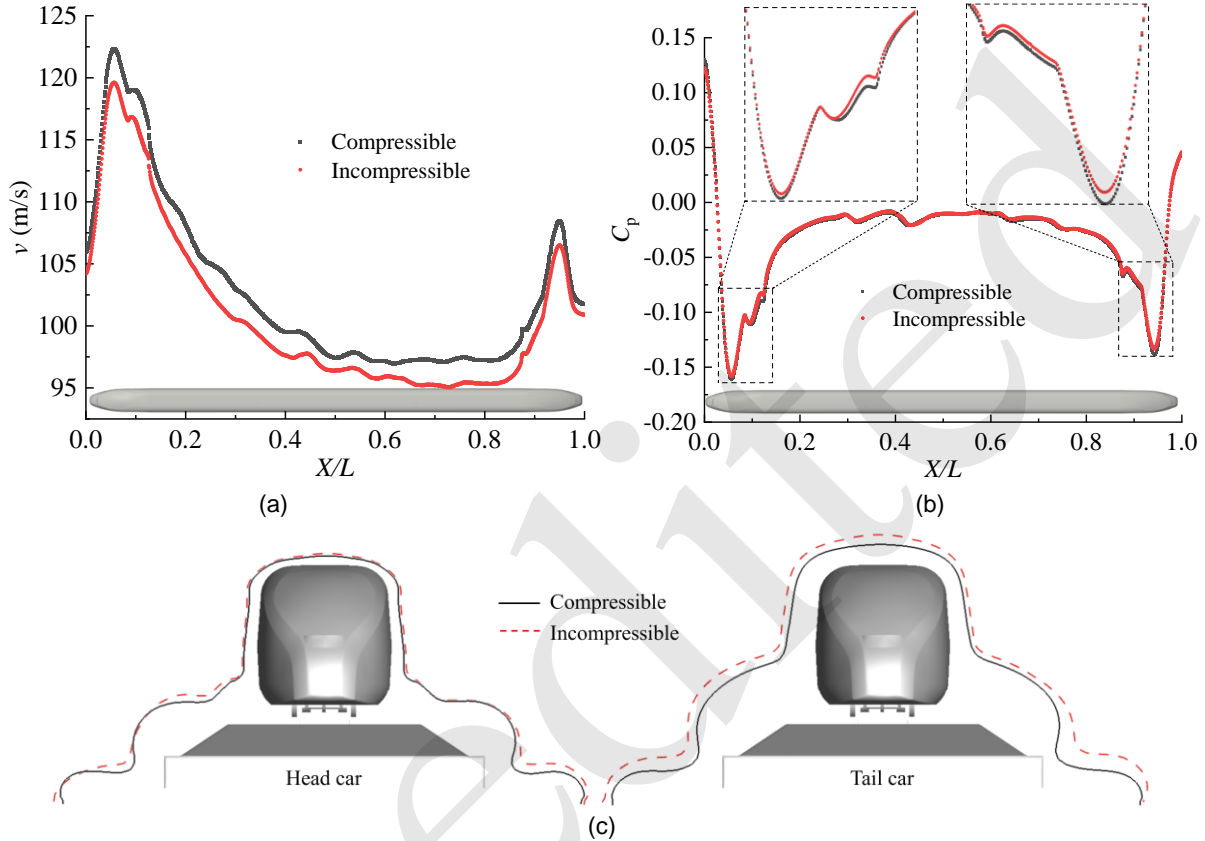


Fig 5 Comparison of compressible and incompressible gases: (a) Velocity distribution of $z = 1.5$ m section (b) Pressure coefficient distribution $z = 1.5$ m section (c) Velocity boundary layer.

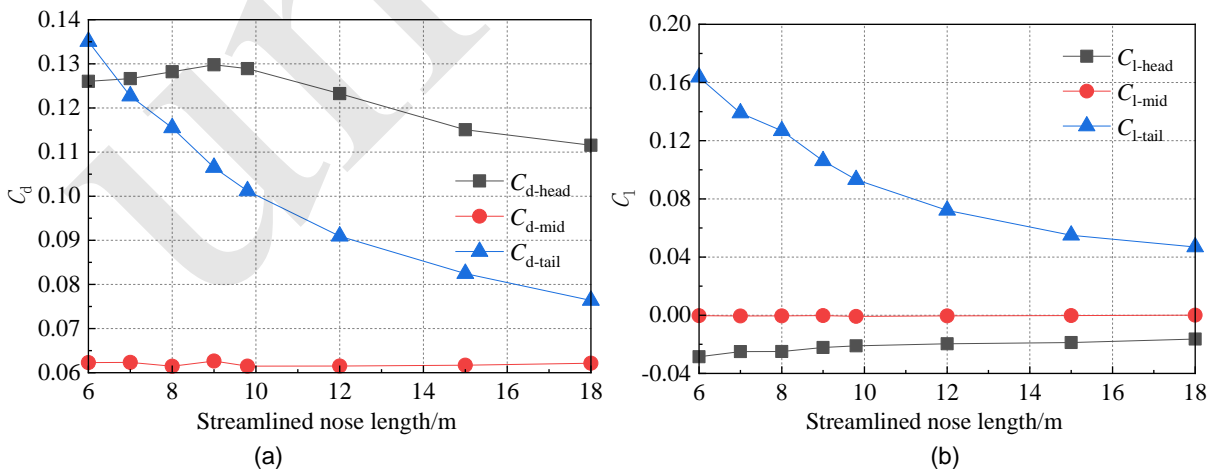


Fig. 6 Changes of aerodynamic force coefficients of each train: (a) Drag coefficient (b) Lift coefficient

4 Numerical Results and Analysis

Fig. 6 illustrates the relationship between the SNL and the aerodynamic force coefficients for each

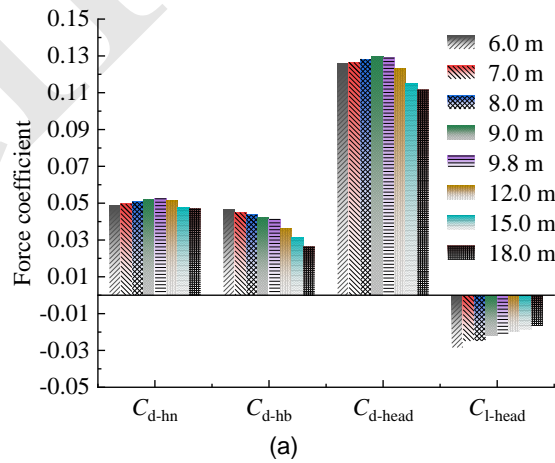
car of the train. It is observed that the aerodynamic force of the middle car is minimally affected by changes in the SNL, resulting in negligible variations in the overall car's aerodynamic force. As a result, the aerodynamic performance of the head and tail cars is the main object of analysis.

4.1 Influence of the SNL on the Aerodynamics of the Head Car

Fig. 7(a) shows the changes in the aerodynamic force coefficients of the head car at the streamlined and non-streamlined parts of different SNLs. If the sign of lift force is negative, it means a downward force and, if it is positive, it means a lift force. In Fig. 7(a), C_{d-hn} represents the drag coefficient of the streamlined part, and C_{d-hb} represents the drag coefficient of the non-streamlined part. According to the data presented in Fig. 7(a), the total resistance exhibits an initial increase followed by a subsequent decrease as the SNL increases. The resistance of the streamlined part follows a similar pattern as the overall resistance of the head car, increasing initially and then decreasing as the SNL increases. However, the resistance of the non-streamlined part decreases as the SNL increases. Additionally, the overall lift force acting on the head car is oriented downward and gradually decreases in magnitude.

The overall resistance is composed of pressure resistance and viscous resistance. Fig. 7(b) shows the changes in the two kinds of resistance of the streamlined part. As the SNL increases, the pressure re-

sistance of the streamlined part exhibits a gradual decrease, while the viscous resistance exhibits a gradual increase and the total resistance first increases and then decreases. The two kinds of resistance changes in the non-streamlined part are shown in Fig. 7(c). The decrease in the resistance of the non-streamlined part is mainly due to the decrease in viscous resistance, while the pressure resistance has almost no change. As shown in Fig. 8(a), the streamlined front end of the head train (i.e. the nose tip) is basically covered by positive pressure because it is located on the windward side. As the SNL increases, the nose tip becomes sharper, the frontal area decreases, and the positive pressure area gradually decreases in both size and extent. Therefore, the integral resistance of the nose tip positive pressure along the running direction gradually decreases, resulting in a decrease of the pressure resistance. As the SNL increases, the contact area between the streamlined part and the air increases, so the viscous resistance between the surface of the train and the air in this part increases gradually. Since the non-streamlined part has no windward slope, the surface pressure resistance is very small, and the main source of resistance is viscous resistance. The length of the corresponding non-streamlined part reduces along with the elongation of the SNL of the head car, and the contact area between the air and the non-streamlined part of the train surface decreases, so the viscous resistance decreases.



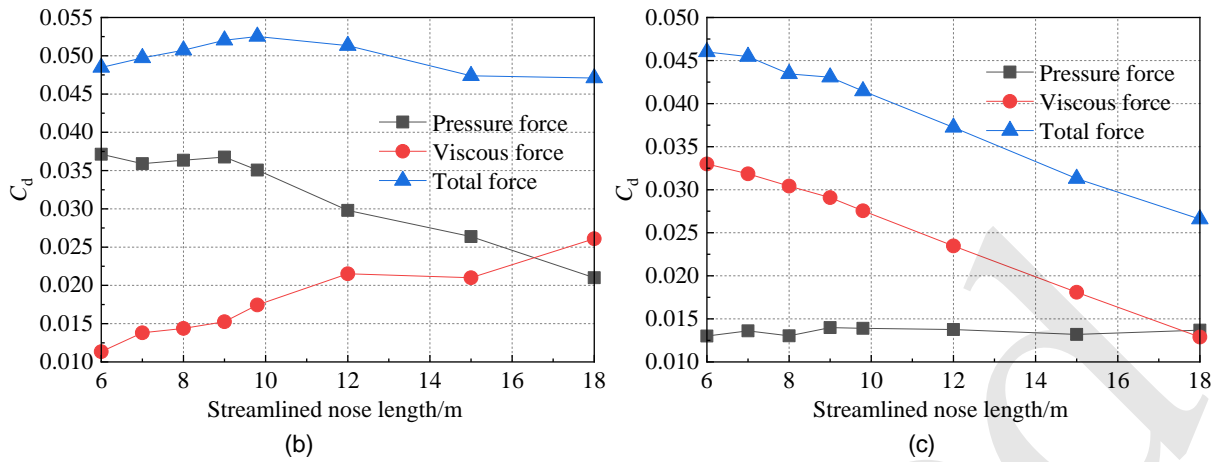
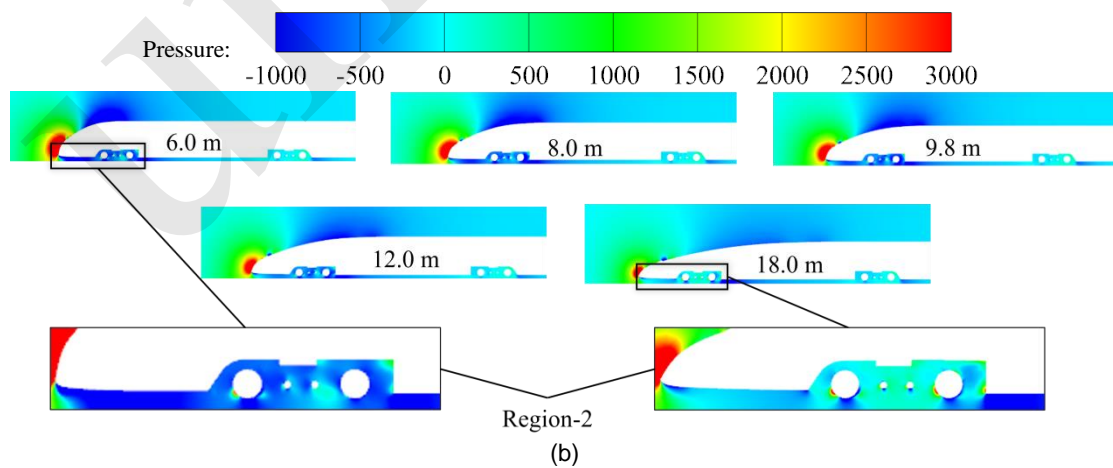
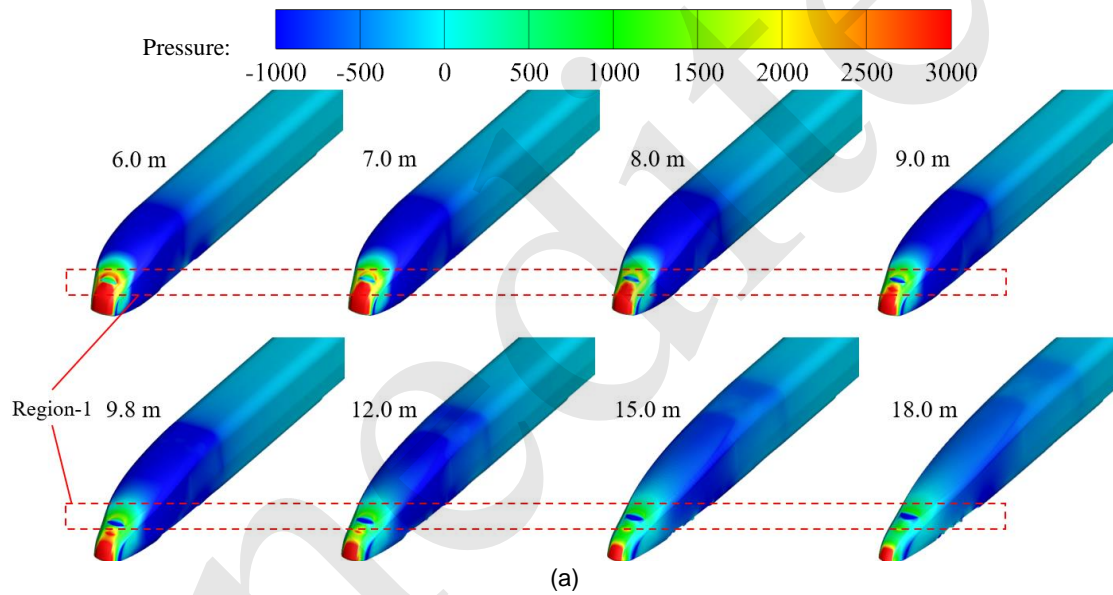


Fig. 7. Changes of aerodynamic force coefficients: (a) Various parts of the head car (b) Drag coefficient of the streamlined part (c) Drag coefficient of the non-streamlined part.



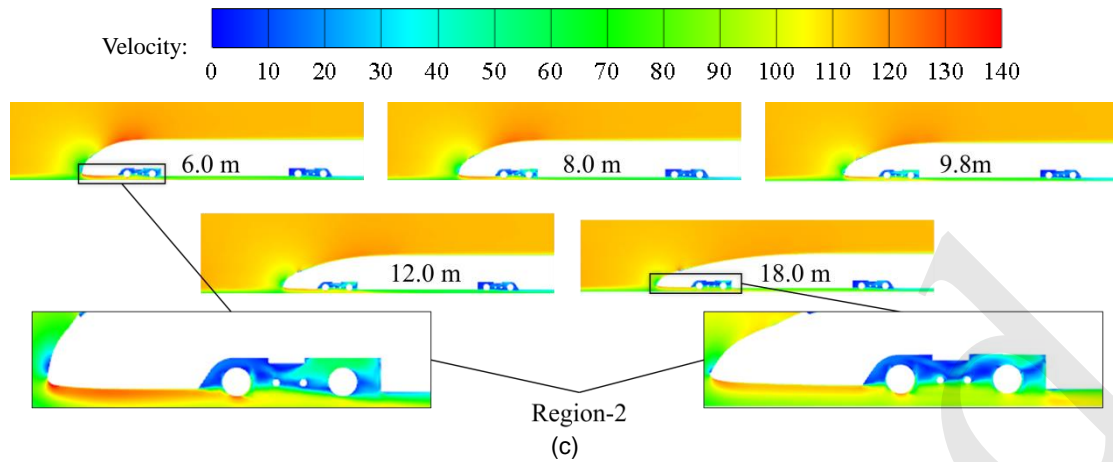


Fig. 8 Distribution of pressure and velocity around the head car: (a) Pressure distribution of the head car surface (b) Pressure distribution of the flow field (c) Velocity distribution of the flow field.

The lift force is predominantly influenced by the positive pressure area located at the nose tip, as well as the negative pressure area that occurs during the transition from the streamlined to the non-streamlined area. As the SNL increases, the vertical downward pressure is weakened, so the downward integral lift force on the head car is reduced. From Region-1 in Fig. 8(a), it can be observed that a longer SNL results in increased airflow being directed towards the rear end of the driver's window as it traverses the concave section. Consequently, the vortex generated in this region progressively grows in size. As a result, the negative pressure area within the recessed part of the driver's window gradually expands, thereby diminishing the downward force exerted. From Fig. 8(b) and Fig. 8(c), the pressure in the bottom of the streamlined nose and the bogie cabin (Region-2) gradually increases. When the streamline is short, the gas in the bottom of the head car is accelerated when it passes through the nose tip, resulting in a high flow velocity, and a large vortex is generated inside the bogie cabin. As the SNL increases, the diversion effect of the head becomes better, and the gas flow velocity in the bottom decreases, leading to a reduction in negative pressure within the bottom area as well as the bogie cabin. Consequently, the upward lift exerted on the train body and the bogie increases, resulting in a decrease in the downforce experienced by the head car.

4.2 Influence of the SNL on the Aerodynamics of the Tail Car

Fig. 9(a) shows the aerodynamic coefficients of

each part of the tail car with different SNLs. In Fig. 9(a), C_{d-tn} represents the drag coefficients of the streamlined part, and C_{d-tb} represents the drag coefficients of the non-streamlined part. As the SNL increases, the total resistance and the total lift both decrease. The resistance changes of the streamlined and non-streamlined parts also show a downward trend.

Fig. 9(b) and Fig. 9(c) show the variation of viscous resistance and pressure resistance in the streamlined and non-streamlined parts, respectively. As the SNL increases, the pressure resistance and total resistance in the streamlined part decrease, while the viscous resistance increases. The viscous resistance of the non-streamlined part decreases but the change range of the pressure resistance is small. The viscous resistance in the non-streamlined part accounts for a large proportion and gradually decreases. The reduction of the pressure value in the negative pressure area results in a reduction in the pressure resistance of the streamlined part, which results in a decrease in the integral resistance of the negative pressure. The increase of viscous drag in the streamlined part is due to the increase in the contact area between the surface of the streamlined body and the air. The velocity boundary layer of the non-streamlined part of each model is shown in Fig. 10(a). As the SNL increases, the thickness of the boundary layer near the surface of the train gradually becomes greater, the average velocity decreases gradually, and the contact area between the surface of the non-streamlined part and the air is reduced, so the viscous resistance and the total resistance of the

non-streamlined part of the tail car are reduced.

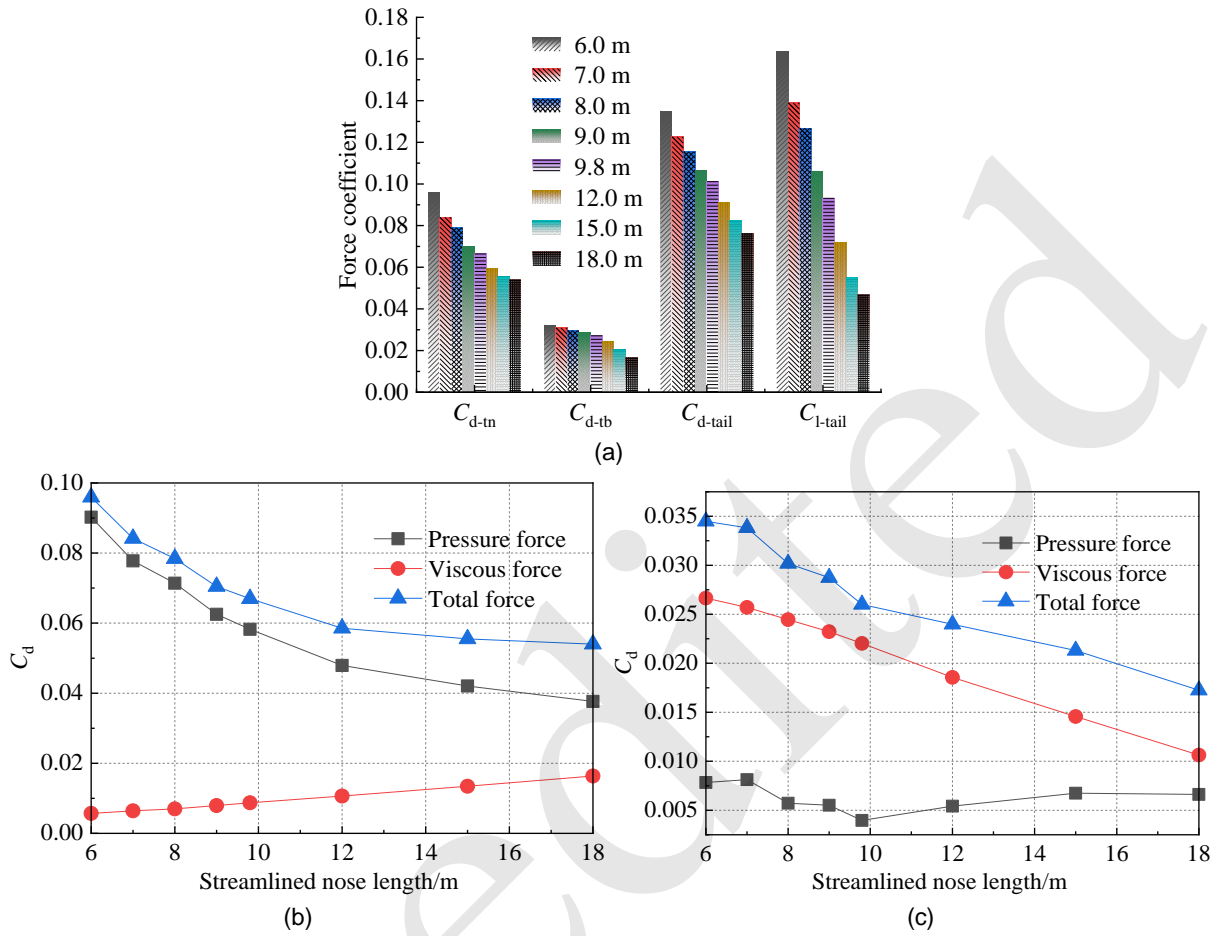
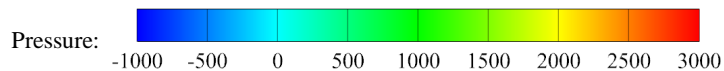
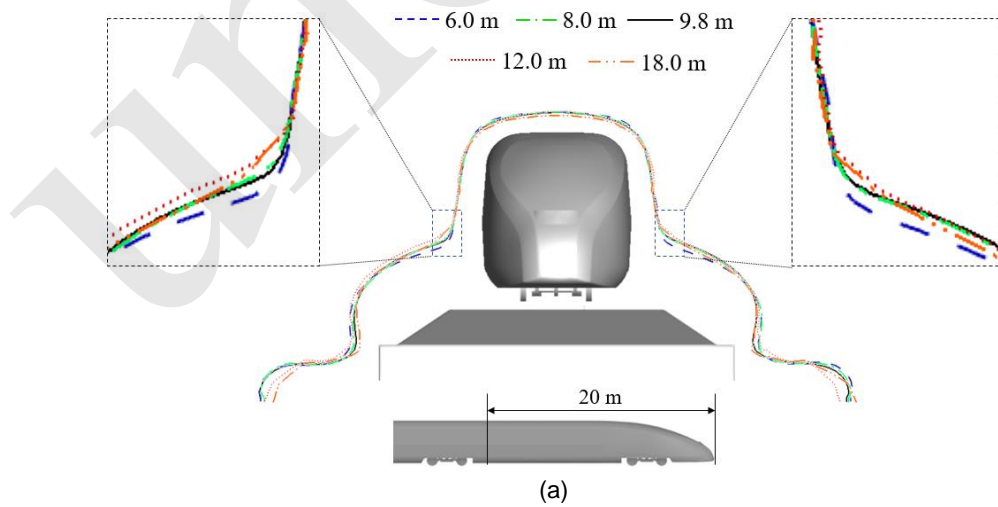


Fig. 9 Changes of aerodynamic force coefficients: (a) Various parts of the tail car (b) Drag coefficient of the streamlined part (c) Drag coefficient of the non-streamlined part.



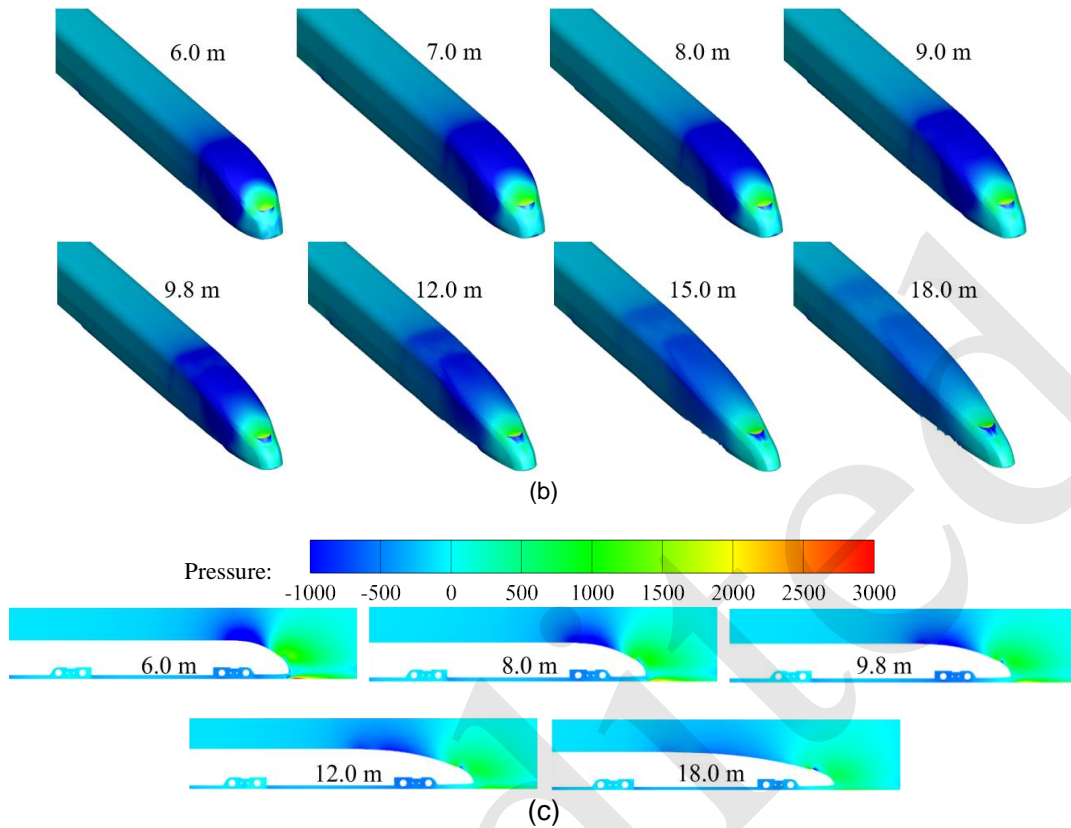


Fig. 10 Velocity boundary layer and pressure distribution of the tail car: (a) velocity boundary layer; (b) pressure distribution of the tail car surface; (c) pressure distribution of the flow field

The change in lift force is primarily influenced by the negative pressure zone formed at the transitional area between the streamlined and non-streamlined sections. Fig. 11 illustrates the variation of the pressure coefficient on the $y = 0$ section. From Fig. 10(b) and Fig. 11, as the SNL becomes longer, the negative pressure absolute value gradually decreases and the vertically upward integral resistance of the tail car decreases, resulting in a decrease in lift. The positive pressure area exhibits relatively stable pressure values, indicating that it has minimal impact on the aerodynamic force variation.

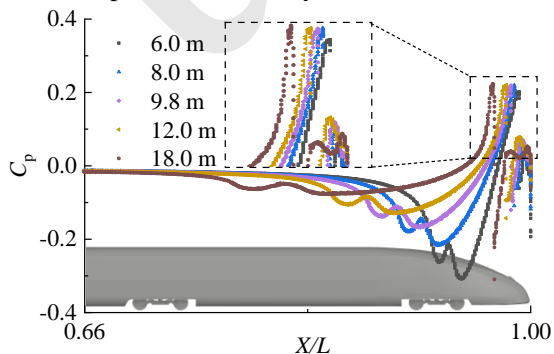


Fig. 11 Distribution of pressure coefficients at $y = 0$ section

of the tail car with different SNLs

4.3 Influence of the SNL on the Surrounding Flow Field

In order to investigate the impact of the SNL on the flow around the train, a monitoring line is defined encircling the train to monitor the pressure and velocity distributions. As shown in Fig. 12(a), the line is parallel to the horizontal of the train, with a height of 1.5 m above the rail surface and a width of 1.7 m referred to the train center. The pressure and velocity distribution along the monitor line are presented in Fig. 12(b) and (c), respectively. The pressure and velocity distribution of the $z = 1.5$ m cross-section are extracted for correlation analysis in Fig. 13.

As depicted in Fig. 12(a), the velocity distribution along Line-1 exhibits significant variations between the streamlined parts while the velocity differences in other sections are relatively minor. As the SNL increases, the peak velocity of the streamlined part decreases; this change can be seen in Region-1 and Region-2 in Fig. 13(a), and the velocity of the wake region of Region-2 also decreases significantly.

The difference in pressure distribution is also mainly reflected in the streamlined part. As the SNL increases, the negative pressure in the streamlined part gradually decreases; this change can be seen in Region-1 and Region-2 in Fig. 13(b). The streamlined nose shape has a strong influence on airflow separation and reattachment points. Compared with the long

streamlined nose, the airflow separation of the short streamlined nose is earlier at the front of the car, and the airflow separation is later at the rear. This results in drastic changes in the airflow at the front and rear of the short streamlined car, with a higher airflow velocity, resulting in greater negative pressure. Increasing the SNL can slow down this airflow change.

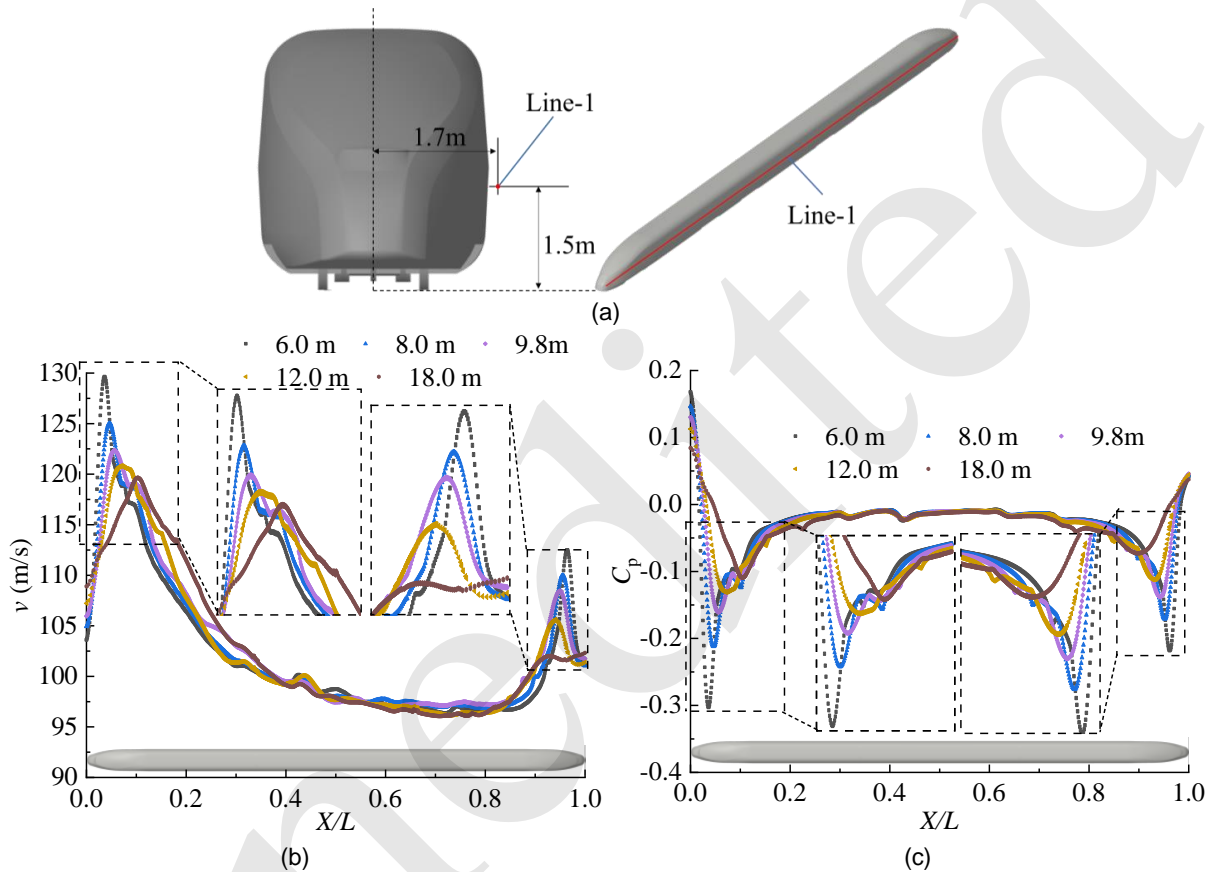
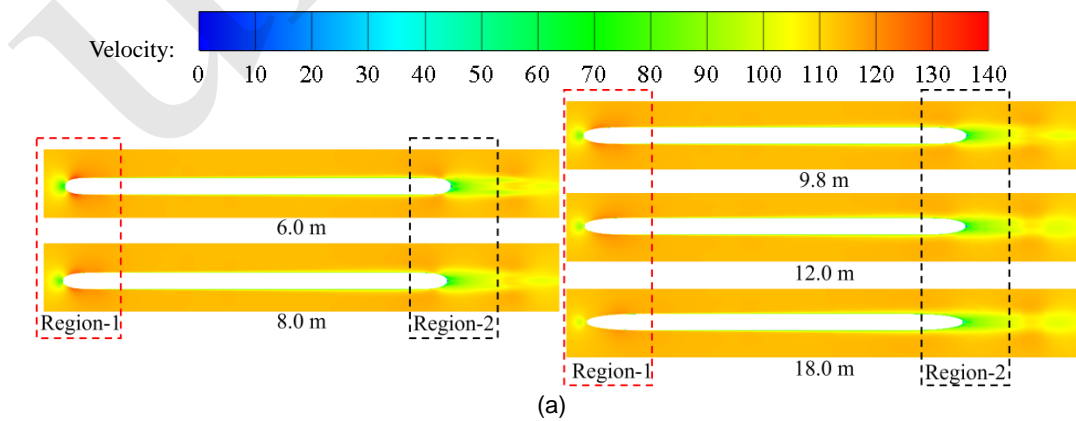


Fig. 12 Velocity and pressure coefficient distribution around the train: (a) The monitor line around the train (b) Velocity distribution (c) Pressure coefficient distribution.



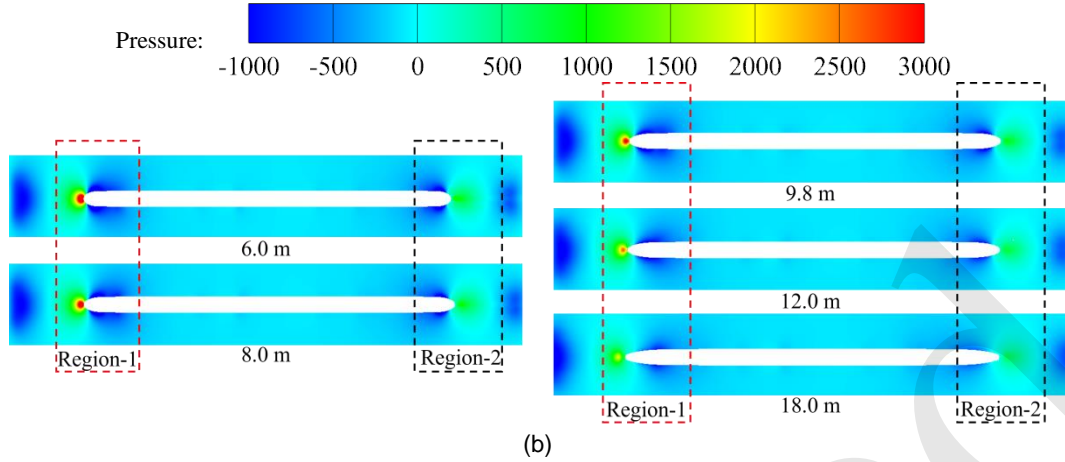


Fig. 13 Velocity and pressure distribution on the $z = 1.5$ m cross-section: (a) Velocity distribution (b) Pressure distribution.

4.4 Aerodynamic Results and Predictions

Table 3 Aerodynamic coefficients of trains with different SNLs

SNL	C_d	$C_{l\text{-head}}$	$C_{l\text{-tail}}$
6.0 m	0.3252	-0.0285	0.1636
7.0 m	0.3135	-0.0250	0.1390
8.0 m	0.3071	-0.0249	0.1268
9.0 m	0.3008	-0.0222	0.1062
9.8 m	0.2935	-0.0210	0.0932
12.0 m	0.2776	-0.0196	0.0721
15.0 m	0.2611	-0.0188	0.0550
18.0 m	0.2520	-0.0164	0.0469

Table 3 shows the aerodynamic coefficients of the whole vehicle with various SNLs. As the SNL increases, the overall resistance of the train decreases. Compared with the primitive car model, the resistance of the train with a 6 m SNL increases by 10.8% and the resistance of the train with an 18 m SNL decreases by 16.5%. The lift of the head and tail cars with a 6 m SNL increases by 35.7% and 75.5%, respectively, and the lift of the head and tail cars with an SNL of 18 m decreases by 21.9% and 49.7%, respectively. Therefore, by elongating the SNL of a train, the aerodynamic performance can be optimized, and the resistance and lift force suffered by the train can be reduced.

According to Li et al. (2019), when the train is operating at a speed of 200 km/h, as the SNL increases from 4m to 7 m, the head car drag coefficient decreases by 17.6%, the tail car drag coefficient decreases by 29.3%, the head car lift force coefficient decreases by 15.8%, and the tail car lift force coefficient decreases by 75.7%. However, the

change in aerodynamic forces is not very obvious when the SNL increases from 7m to 12m. In this study, when the running speed of the train reaches 400 km/h, the aerodynamic forces change significantly as the SNL increases from 6 m to 18 m. Therefore, the SNL of the train at that speed has a great impact on the aerodynamic performance of the train.

Analyzing the drag coefficient of the whole train and the lift coefficient of the tail car, it can be observed that the drag of the whole train and the lift of the tail car have respectively linear and quadratic function relationships with the SNL. Therefore, the following predictive formulas for train resistance and tail car lift coefficient can be obtained by using first-order and second-order polynomial fitting:

$$C_d = C_{d\text{-head}} + C_{d\text{-tail}} + C_{d\text{-mid}} \quad (4)$$

$$= (-0.0061x + 0.2944) + 0.0619$$

$$C_{l\text{-tail}} = 0.00093x^2 - 0.0318x + 0.3186; \quad (5)$$

where x is the SNL of the train; C_d and $C_{l\text{-tail}}$ are the drag coefficient of the whole train and the lift coefficient of the tail train, respectively.

Since the resistance of the middle car is basically unchanged, the average value of the drag coefficient of the middle car is expressed in the fitting formula as a separate constant. The linear function in the brackets of the first term in formula (4) is the fitted drag coefficient formula of the head car and tail car, the second constant is the average drag coefficient of the middle car.

Table 4 Statistics for fitting formulas

	C_d	C_{l-tail}
R^2	0.9755	0.9958
Residual mean	-2.1×10^{-6}	-2.2×10^{-6}
RMSE	3.76×10^{-3}	2.50×10^{-3}

As shown in Table 4, according to the analysis of the fitting formulas, the R^2 of the two fitting formulas are 0.9755 and 0.9958, which are close to 1, both the residual mean value and the root mean square error (RMSE) of the fitting formulas are close to zero. It

can be seen from Fig. 14 that the original data points of the aerodynamic force coefficient are basically distributed around the fitting curve and the residuals of different data points are randomly distributed around zero; the maximum residual of C_d is only 0.006, the relative error is less than 3%, and the maximum residual of C_{l-tail} is only 0.003, the relative error is less than 2%. Therefore, under the condition that the Reynolds number is about 2.8×10^7 , the fitting formula can be used to predict the aerodynamic force of trains with SNL in the range of 6 to 18 m.

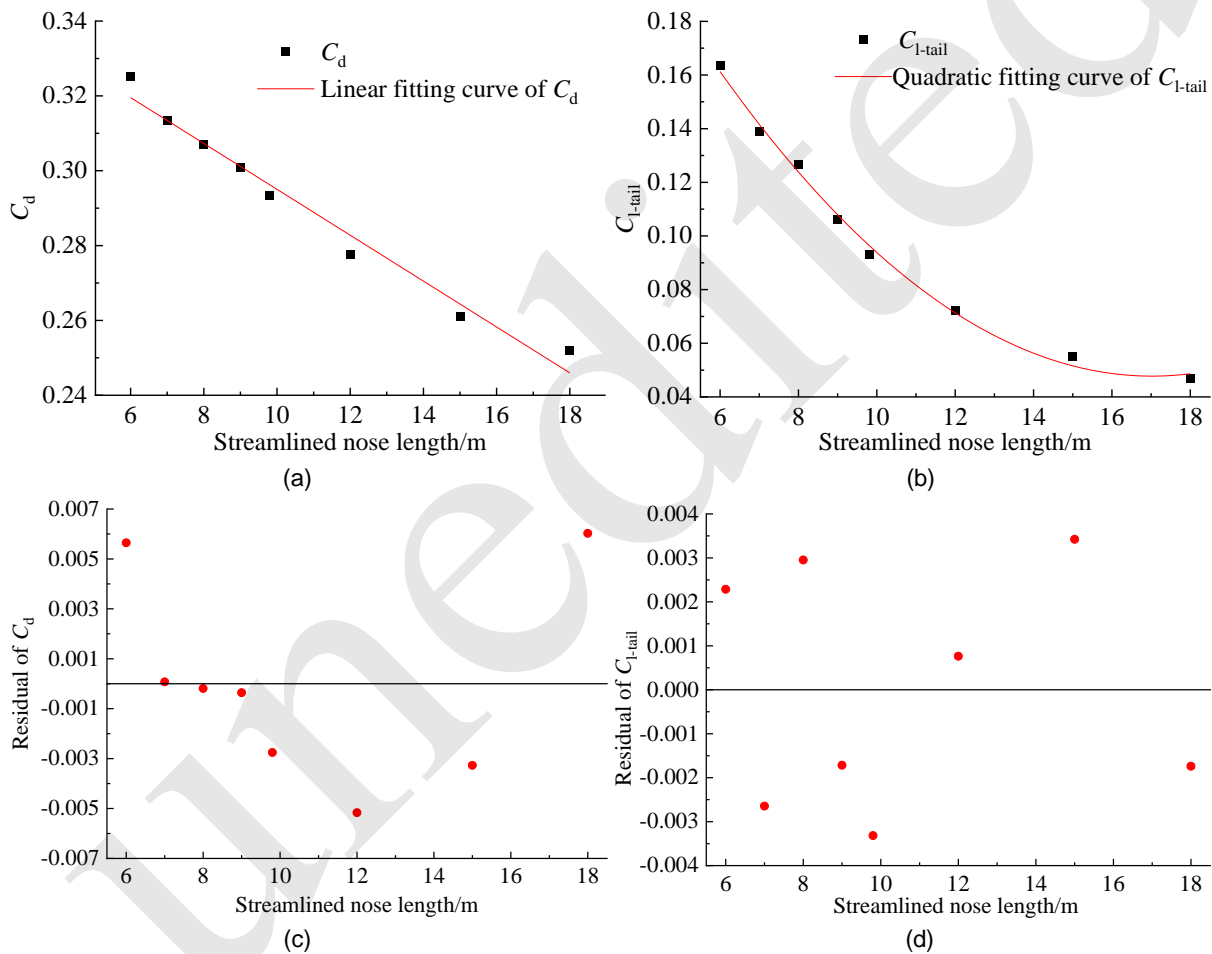


Fig. 14 Fitting curve and residual: (a) Fitting curve of C_d (b) Fitting curve of C_{l-tail} (c) Residual distribution of C_d (d) Residual distribution of C_{l-tail} .

5 Conclusions

This paper investigates the aerodynamic performance of high-speed trains operating at a speed of 400km/h, mainly studying the impact of the SNL of the train on the aerodynamic performance of the train

at this speed level. The main conclusions obtained are the following:

1. Numerical simulations are performed with compressible and incompressible gases to validate the effect of gas compressibility on results. The relative error of the drag force of the head car is 4.3%, and the maximum absolute error of velocity value and aero-

dynamic force value of the flow field around the train reached 3.22 m/s and 702 N, respectively. This validates the feasibility and rationality of using compressible gas in the numerical simulation of train aerodynamic performance in this study.

2. As the SNL increases, the pressure resistance of the streamlined part of the head car gradually decreases, and the viscous resistance gradually increases. The pressure resistance of the non-streamlined part is unchanged, the viscous resistance gradually decreases, and the overall aerodynamic resistance of the head car increases first and then decreases. The aerodynamic lift of the head car is expressed as a downforce, which decreases as the increase in SNL.

3. As the SNL increases, the pressure resistance of the streamlined part of the tail car gradually decreases and the viscous resistance gradually increases. The changing amplitude of the pressure resistance in the non-streamlined part is small, the viscous resistance gradually decreases, and the overall aerodynamic resistance of the tail car is decreased. The overall aerodynamic lift of the tail car decreases.

4. When the SNL is reduced from 9.8 m to 6 m, the train experiences an increase of 10.8% in aerodynamic drag. Additionally, the lift forces on the head car and tail car are increased by 35.7% and 75.5% respectively. Conversely, when the SNL is increased from 9.8 m to 18 m, the train experienced a decrease of 16.5% in aerodynamic drag. The lift forces on the head car and tail car decreased by 21.9% and 49.7% respectively. The relationship between the SNL and the aerodynamic forces can be approximated using fitting formulas.

Acknowledgments

This work was supported by National Natural Science Foundation of China (12372049), Sichuan Science and Technology Program (2023JDRC0062) and the Independent Project of State Key Laboratory of Rail Transit Vehicle System (2023TPL-T06) and the Fundamental Research Funds for the Central Universities (2682023ZTPY036).

Declaration of Conflicting Interests

The authors declare that they have no conflicts of

interest to report regarding the present study.

References

- Britcher CP, Wells JM, Renaud B, et al., 2012. Aerodynamics of urban maglev vehicles. *Proceedings of the Institution of Mechanical Engineers, Part F: Journal of Rail and Rapid Transit*, 226(6):561-567.
- Chen G, Li XB, Liu Z, et al., 2019. Dynamic analysis of the effect of nose length on train aerodynamic performance. *Journal of Wind Engineering and Industrial Aerodynamics*, 184:198-208.
- Chen ZW, Liu TH, Jiang ZH, et al., 2018. Comparative analysis of the effect of different nose lengths on train aerodynamic performance under crosswind. *Journal of Fluids and Structures*, 78:69-85.
- Choi JK, Kim KH, 2014. Effects of nose shape and tunnel cross-sectional area on aerodynamic drag of train traveling in tunnels. *Tunnelling and Underground Space Technology*, 41:62-73.
- Dai ZY, Li T, Zhang WH, et al., 2023. Research progress of aerodynamic multi-objective optimization on high-speed train nose shape. *CMES-Computer Modeling in Engineering & Sciences*, 137(2)
- Ezaji R, Talaei MR, 2021. Analysis of overturn of high-speed train with various nose shapes under crosswind. *Iranian Journal of Science and Technology, Transactions of Mechanical Engineering*, 46: 297–310.
- Hu X, Deng ZG, Zhang JW, et al., 2022. Aerodynamic behaviors in supersonic evacuated tube transportation with different train nose lengths. *International Journal of Heat and Mass Transfer*, 183:122130.
- Huang S, Li ZW, Yang MZ, 2019. Aerodynamics of high-speed maglev trains passing each other in open air. *Journal of Wind Engineering and Industrial Aerodynamics*, 188:151-160.
- Huo XS, Liu TH, Chen ZW, et al., 2021. Comparative analysis of the aerodynamic characteristics on double-unit trains formed by different types of high-speed train. *Journal of Wind Engineering and Industrial Aerodynamics*, 217:104757.
- Iglesias EL, Thompson D, Smith M, 2017. Component-based model to predict aerodynamic noise from high-speed train pantographs. *Journal of Sound and Vibration*, 394:280-305.
- Kikuchi K, Iida M, Fukuda T, 2011. Optimization of train nose shape for reducing micro-pressure wave radiated from tunnel exit. *Journal of Low Frequency Noise, Vibration and Active Control*, 30(1):1-19.
- Kim TK, Kim KH, Kwon HB, 2011. Aerodynamic characteristics of a tube train. *Journal of Wind Engineering and Industrial Aerodynamics*, 99(12):1187-1196.
- Li T, Liang H, Zhang JY, et al., 2023. Numerical study on aerodynamic resistance reduction of high-speed train using vortex generator. *Engineering Applications of Computational Fluid Mechanics*, 17(1):e2153925.

- Li T, Qin D, Zhou N, et al., 2022. Step-by-step numerical prediction of aerodynamic noise generated by high speed trains. *Chinese Journal of Mechanical Engineering*, 35(1):28.
- Li T, Zhang JY, Zhang WH, 2013. A numerical approach to the interaction between airflow and a high-speed train subjected to crosswind. *Journal of Zhejiang University Science A*, 14(7):482-493.
- Li XL, Chen G, Zhou D, et al., 2019. Impact of different nose lengths on flow-field structure around a high-speed train. *Applied Sciences*, 9(21): 4573.
- Li XH, Deng J, Chen DW, et al., 2011. Unsteady simulation for a high-speed train entering a tunnel. *Journal of Zhejiang University-SCIENCE A*, 12(12):957-963.
- Liu X, Deng J, Zheng Y, et al., 2013. Impact of aerodynamics of pantograph of a high-speed train on pantograph-catenary current collection. *Journal of Zhejiang University. Engineering Science*, 47(3):558-564.
- Meng S, Zhou D, Xiong XH, et al., 2022. The effect of the nose length on the aerodynamics of a high-speed train passing through a noise barrier. *Flow, Turbulence and Combustion*, 108(2):411-431.
- Miao XJ, Gao GJ, Wang JB, et al., 2023. Effect of low operating temperature on the aerodynamic characteristics of a high-speed train. *Journal of Zhejiang University-SCIENCE A*, 24(3):284-298.
- Niu JQ, Wang YM, Zhang L, et al., 2018. Numerical analysis of aerodynamic characteristics of high-speed train with different train nose lengths. *International Journal of Heat and Mass Transfer*, 127:188-199.
- Raghunathan RS, Kim HD, Setoguchi T, 2002. Aerodynamics of high-speed railway train. *Progress in Aerospace sciences*, 38(6-7):469-514.
- Shao XM, Wan J, Chen DW, et al., 2011. Aerodynamic modeling and stability analysis of a high-speed train under strong rain and crosswind conditions. *Journal of Zhejiang University-SCIENCE A*, 12(12):964-970.
- Sun ZX, Wang MY, Wei LY, et al., 2021. Aerodynamic shape optimization of an urban maglev train. *Acta Mechanica Sinica*, 37(6):954-969.
- White FM, Majdalani J, 2006. *Viscous fluid flow. translators, McGraw-Hill New York*, 24.
- Xiao YG, Qun Y, Sun L, et al., 2014. Longitudinal type-line optimization of high-speed train for low aerodynamic noise. *Journal of Central South University*, 21(6):2494-2500.
- Xiong HB, Yu WG, Chen DW, et al., 2011. Numerical study on the aerodynamic performance and safe running of high-speed trains in sandstorms. *Journal of Zhejiang University-SCIENCE A*, 12(12):971-978.
- Yu MG, Zhang JY, Zhang WH, 2013. Multi-objective optimization design method of the high-speed train head. *Journal of Zhejiang University Science A*, 14(9):631-641.
- Zampieri A, Rocchi D, Schito P, et al., 2020. Numerical-experimental analysis of the slipstream

produced by a high speed train. *Journal of Wind Engineering and Industrial Aerodynamics*, 196:104022.

Zhang L, Zhang JY, Li T, et al., 2017. Multi-objective aerodynamic optimization design of high-speed train head shape. *Journal of Zhejiang University-SCIENCE A*, 18(11):841-854.

Zhang XH, Jiang Y, Li T, 2020. Effect of streamlined nose length on the aerodynamic performance of a 800 km/h evacuated tube train. *Fluid Dynamics & Materials Processing*, 16(1):67-76.

中文概要

题目: 流线型车头长度对 400 km/h 高速列车气动性能的影响

作者: 李念勋, 李田, 戴志远, 秦登, 张继业

机构: 西南交通大学, 轨道交通运载系统全国重点实验室, 中国成都, 610031

目的: 通过对时速 400 公里、具有不同流线型车头长度的高速列车的空气动力性能进行数值模拟, 分析其流线型长度对高速列车的气动性能的影响, 对高速列车的头型优化给出建议。

创新点: 1. 考虑空气的可压缩性, 研究列车以时速 400 km/h 运行时的气动性能; 2. 分析了列车的气动力变化规律, 得到了可适用于流线型长度在 6 到 18 m 之间的列车气动力拟合公式。

方法: 1. 通过将仿真结果与已有的风洞试验数据进行对比, 验证了数值模拟的可行性与准确性; 2. 分别对比采用可压缩气体和不可压缩气体进行数值模拟的结果, 说明采用可压缩气体进行数值仿真的准确性; 3. 对列车的气动力、边界层及周围流场进行分析, 得到了流线型长度对列车气动性能的影响。

结论: 1. 分别采用可压缩和不可压缩气体进行数值模拟, 验证气体压缩性对结果的影响。头车阻力相对误差为 4.3%, 这验证了本研究中可使用可压缩气体进行列车气动性能数值模拟的可行性和合理性; 2. 随着流线型长度的增大, 头车和尾车的气动阻力都有所减小, 头车向下的升力和尾车向上的升力均有所减小; 3. 当流线型长度从 9.8 m 减小到 6 m 时, 列车的气动阻力增加了 10.8%。此外, 头车和尾车的升力分别增加了 35.7% 和 75.5%。相反, 当流线型长度从 9.8 m 增加到 18 m 时, 列车的气动阻力下降了 16.5%。头车、尾车升力分别下降 21.9%、49.7%。流线型长度和气动力的关系可以使用拟合公式来表示。

关键词：流线型车头长度；高速列车；空气动力学性能；
数值模拟；流动结构

Unedited